Detailed crustal deformation in the Ailaoshan Orogenic Belt revealed by receiver functions from a dense array

Chenglong Wu[1,2], Tao Xu[1,2]* and Zhiming Bai[3,2]

[1]Key Laboratory of Mineral Resources, Institute of Geology and Geophysics, Chinese Academy of Sciences, Beijing, China, [2]Innovation Academy for Earth Science, Chinese Academy of Sciences, Beijing, China, [3]State Key Laboratory of Lithospheric Evolution, Institute of Geology and Geophysics, Chinese Academy of Sciences, Beijing, China

The Ailaoshan Orogenic Belt (AOB), located at the southeastern boundary of the Tibetan Plateau, is an ideal place for investigating the mechanisms of lateral growth of Tibet. Using the data recorded by a dense seismic array across the Ailaoshan belt, we investigate the detailed lateral variations of crustal anisotropy on the basis of Pms phase of receiver functions. Remarkable crustal anisotropy is observed throughout this study region with a mean delay time of 0.33 ± 0.19 s, indicating the anisotropy primarily originates in the middle-lower crust. The fast directions beneath the AOB including the Ailaoshan-Red River shear zone (ARRSZ) and its western low-grade metamorphic unit generally align with the NW-SE strike of ARRSZ. The weak anisotropy in the South China Block (SCB) argues that the block is relatively stable, with limited internal deformation. Meanwhile, the anisotropy beneath the western boundary of the SCB is strong, and the N-S oriented fast direction is influenced by both the crustal stress and Xiaojiang Fault. Combining the high Vp/Vs and significant lateral variations of crustal anisotropy parameters, we suggest that the strike-slip motion along the ARRSZ induces the partial melting and pronounced anisotropy in the middle-lower crust of AOB, without the presence of crustal flow. The differences between crustal and mantle anisotropy indicate crust-mantle decoupling deformation of the AOB, supporting the block extrusion model occurring only in the crustal scale as the primary deformation pattern.

KEYWORDS

crustal anisotropy, receiver function, crustal deformation, Ailaoshan Orogenic Belt, decoupling between crust and upper mantle, Southeastern Tibet

1 Introduction

The Tibetan Plateau has served as a prime example of a continental collision between the Eurasian and Indian plates since around 60 million years ago (Yin and Harrison, 2000). Various geodynamic models were presented to elucidate the formation and sustenance of high topography of Tibet. These models encompass the lateral extrusion of continental lithosphere along major strike-slip faults bounding the plateau (Tapponnier et al., 2001), crustal flow effectively decoupling the crustal deformation from the mantle (Clark and Royden, 2000), and a thin viscous sheet where the plateau experiences distributed shortening (England and McKenzie, 1982). The Ailaoshan Orogenic Belt is located in the southeastern Tibet, and containing the Ailaoshan-Red River shear zone (ARRSZ) which is the boundary

between the South China and the Indochina Blocks. Thus this area provides an excellent setting to investigate the mechanisms of plateau lateral growth.

Crustal anisotropy can provide key information of crustal deformation, and typically comprises two main types, stress-induced anisotropy and structural anisotropy (Boness and Zoback, 2006). The upper crustal anisotropy is primarily linked to the dilation of microcracks, leading to a fast polarization orientation aligned with S_{Hmax} (Crampin, 1991). This type of stress-induced anisotropy exists primarily within the upper crust and diminishes as the depth increases due to closure of micro-cracks. Alternatively, structural anisotropy arises from aligned macroscopic fractures, fault fabrics and anisotropic minerals' lattice preferred orientation (LPO), which commonly contributes to the anisotropy of the middle-lower crust. Some studies have already utilized the Pms phase of the Moho to obtain anisotropy within the crust and related deformation characteristics in southeastern Tibet. Sun et al. (2012) suggested the existence of crustal flow based on the large splitting times. Chen et al. (2013) asserted that the southeastward crustal flow within the plateau reaches the Lijiang-Xiaojinhe Fault, but it is hindered by the Central Yunan Block further to the south. While Shi et al. (2023) suggested that the SE oriented ductile flow is likely prevented by the high-velocity zones beneath Emeishan large igneous province. With more data of ChinArray, Cai et al. (2016) found near the major faults, the crust deformation is dominantly due to strike-slip motion. In addition, Yang et al. (2022) argued that the southeastern Tibetan Plateau experienced tectonic extension rather than crustal shortening and thickening within the plateau. The deformation pattern of the Tibetan Plateau still remains highly contentious. Previous studies could not provide small-scale lateral variations in crustal anisotropy within critical tectonic zones such as the Ailaoshan belt due to large station spacing greater than 30 km.

Recently, a dense seismic array with a mean station spacing of 500 m installed across the Ailaoshan belt is employed to obtain the crustal structure by receiver function (RF) method (Zhang et al., 2020). In this work, the crustal anisotropy parameters are measured based on the Pms phase from RFs. Our new findings offer detailed spatial variations of the local anisotropy parameters and fresh perspectives on the crustal deformation within the Ailaoshan belt in southeastern Tibet.

2 Data and methods

2.1 Data

The data for the investigation were obtained from a dense seismic array installed in the southeastern Tibet (Zhang et al., 2020; Zheng et al., 2021). The roughly east-west array spans three tectonic regions, namely, the Lanping-Simao Basin, the Ailaoshan Orogenic Belt, and the South China Block (Figure 1). Totally 480 seismic stations were installed at consisting of 118 EPS and 362 PDS-2 short-period seismic sensors spaced at 0.5 km intervals. The experiment, extending from December 2017 to January 2018, lasted for 35 days. From the original data, a total of 31 earthquakes with magnitudes exceeding 5.2 and epicentral distances ranging from 28° to 95° were selected. These events offer a

good back-azimuthal coverage despite the short observation period (Zhang et al., 2020).

Initially, the raw data underwent band-pass filtration between 0.05–5.0 Hz. The horizontal components were rotated to create radial and transverse components. We generated the radial RFs utilizing the time-domain iterative deconvolution with a Gaussian value of 5.0. The RFs with ambiguous Pms arrivals were excluded by visual inspection. Finally, a total of 1,588 RFs were gathered (Zhang et al., 2020).

2.2 Detection of one layered anisotropy

A range of techniques have been used to study crustal anisotropy, including local S splitting (Gao et al., 2011; Wu et al., 2019), Pms splitting (Chen et al., 2013), and sinusoidal moveout of Pms (Liu and Niu, 2012; Rümpker et al., 2014). The last one has gained popularity during the recent period because this approach may avoid the instability associated with event-by-event processing. Under the assumption of one anisotropic layer possessing a horizontally oriented axis of symmetry, the Pms arrival time varies following a cosine function of the earthquake's back-azimuth (Baz) (Liu and Niu, 2012) and can be stated as:

$$t_{Pms} = t_0 - \frac{\delta t}{2} \cos[2(\alpha - \varphi)] \qquad (1)$$

In the Eq. 1, t_0 is the isotropic Pms arrival time, δt indicates the time delay between the slow wave and fast wave, φ is the fast direction calculated clockwise from the north, and α denotes the earthquake event's Baz.

Some studies suggest that the dipping Moho would cause the azimuthal variations in the Pms delays (Li et al., 2019). By numerical tests, Wu et al. (2021) found that the systematic moveout method could get consistent splitting parameters with the theoretical values with the dipping angle less than 10°. The Moho depth in the study area varies from 36.2 km to 38.5 km, showing no notable undulations (Zhang et al., 2020), thus the approach is suitable in the study region.

Before utilizing Eq. 1, we follow the procedures for preprocessing the RFs to improve the accuracy of the measurements. Firstly, to minimize the moveout caused by epicentral distances, all RFs were adjusted to a consistent ray parameter of 0.06 s/km utilizing the IASP91 model (Kennett and Engdahl, 1991). Secondly, considering this dense array with limited useful RFs in a single station, we stored the RFs of the 21 nearby stations for the center stations. The center stations are spaced at intervals of 10 stations. Because of the sparse distribution between stations 1,240 and 1,270, we only stored the RFs of the 11 nearby stations for the center stations. At last, the RFs within identical band of Baz were stacked.

A grid research is carried out to get the best measurement with the maximum stacking amplitude. According to the Moho depth and crustal anisotropy obtained from other studies (Cai et al., 2016; Zhang et al., 2020), the searching range for t_0 spans from 4.0 s to 6.0 s in 0.1 s increments, while the ranges for φ and δt are 0°–180° with a 1° interval and 0.0–1.5 s with a 0.01 s increment, respectively. Figures 2, 3 show two examples of measurements for single layered azimuthal anisotropy. The measurements with a delay time larger than 0.5 s are shown in Supplementary Figures S1–S5.
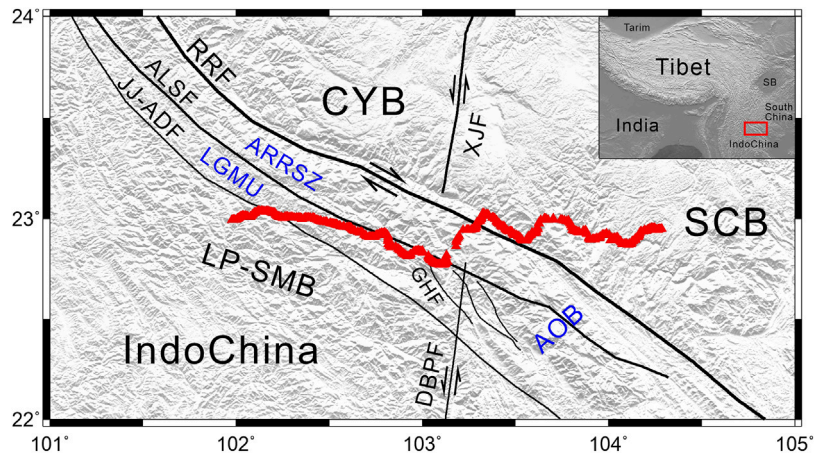
FIGURE 1
Topographic map including faults and seismic stations (depicted as red triangles) within the study area. RRF, Red River Fault; ALSF, Ailaoshan Fault; JJ-ADF, Jiujia-Anding Fault; XJF, Xiaojiang Fault; GHF, Ganhe Fault; DBPF, Dien Bien Phu Fault; CYB, Central Yunnan Block; SCB, South China Block; LP-SMB, Lanping-Simao Basin; AOB, Ailaoshan Orogenic Belt; ARRSZ, Ailaoshan-Red River shear zone; LGMU, low-grade metamorphic unit. The red rectangle in the inset shows the study area. SB, Sichuan Basin.
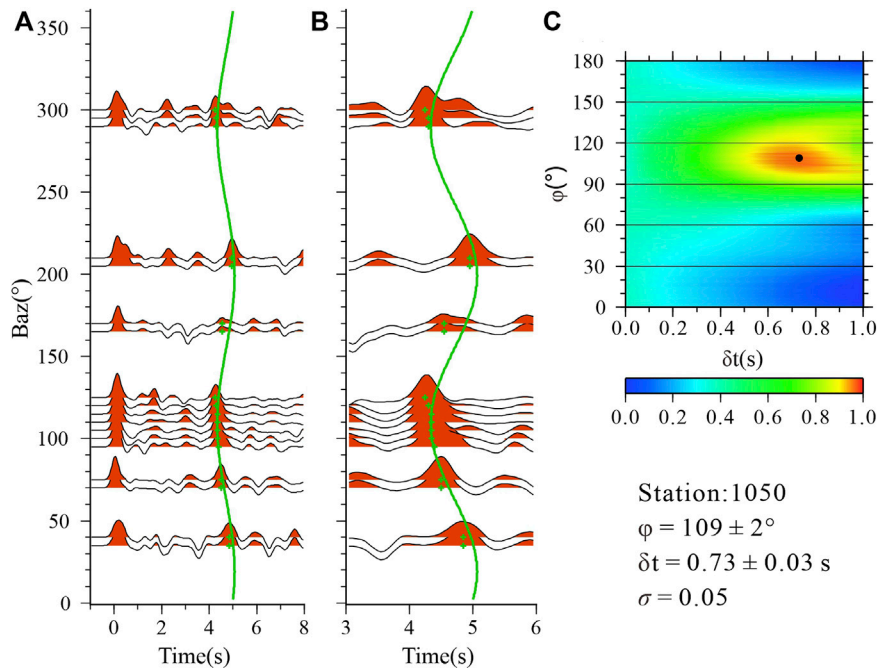

FIGURE 2
Crustal anisotropy measurements for station 1050. **(A)** RF averages for Baz bands plotted against Baz. Green crosses denote the arrivals of Pms. The green line indicates the arrivals of Pms estimated by the best pair of crustal anisotropy results. **(B)** Zoomed-in RFs. **(C)** Stacking amplitudes corresponding to all potential splitting parameters. The black dot represents the best set of crustal anisotropy measurements corresponding to the maximal amplitudes.

2.3 Detection of double layered anisotropy

The layer-stripping approach (Rümpker et al., 2014; Tan and Nie, 2021) can quantify anisotropy above an intracrustal discontinuity for stations that exhibit a clear intracrustal discontinuity, which generates the P-to-S conversion Pis. For stations where both Pms and Pis were observed, we initially utilized the Pis to measure the upper crustal anisotropy. Then, we corrected the Pms arrival times, which account for the cumulative effects of anisotropy within the entire crust, utilizing the splitting results for the upper crust. After eliminating the influence from the upper crustal anisotropy, we use Eq. 1 to evaluate the lower crustal anisotropy based on the modified Pms phases. To ensure the reliability of the two-layered anisotropy
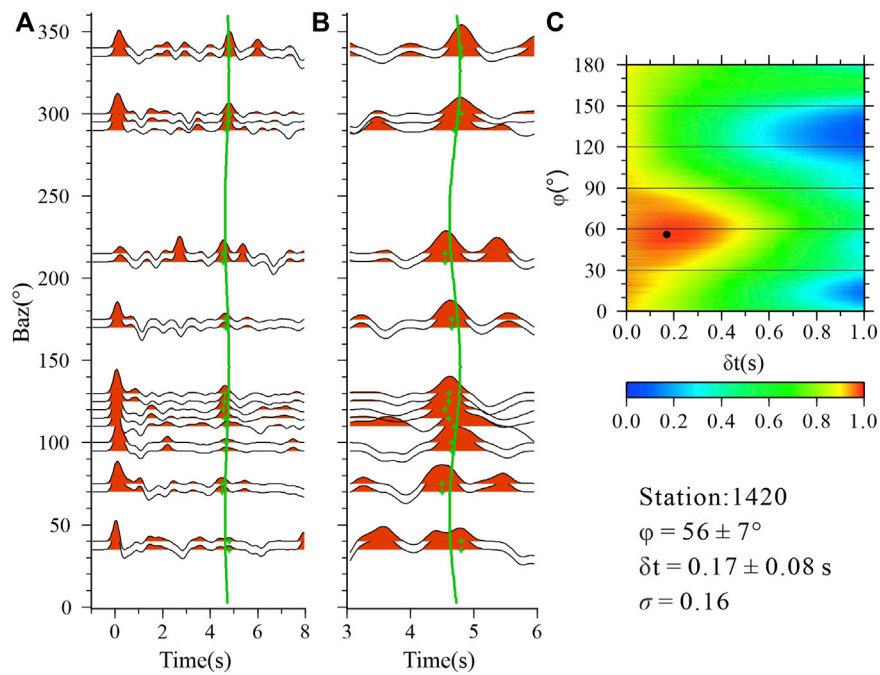
FIGURE 3
Crustal anisotropy measurements for station 1420. **(A)** RF averages for Baz bands plotted against Baz. Green crosses denote the arrivals of Pms. The green line indicates the arrivals of Pms estimated by the best pair of crustal anisotropy results. **(B)** Zoomed-in RFs. **(C)** Stacking amplitudes corresponding to all potential splitting parameters. The black dot represents the best set of crustal anisotropy measurements corresponding to the maximal amplitudes.
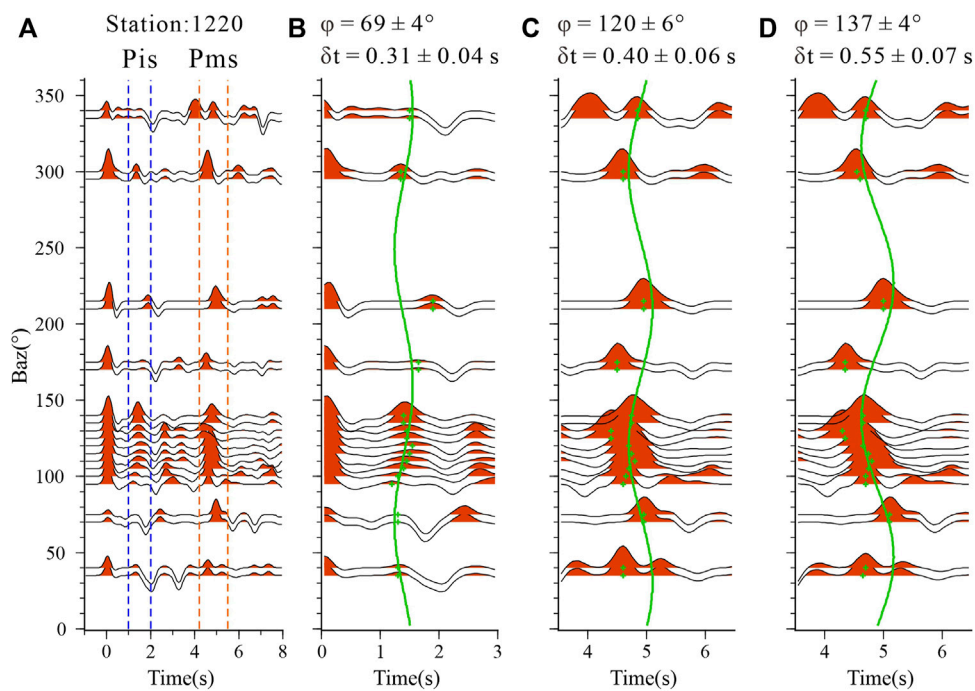
FIGURE 4
Two layered crustal anisotropy analysis for station 1,220. **(A)** RF averages for Baz bands plotted against Baz. Pis and Pms phases are shown within the blue dashed lines and orange dashed lines, respectively. **(B)** Green crosses are the Pis arrivals. The green line indicates the Pis arrivals estimated using the best pair of anisotropy results of the Pis phase. **(C)** The green line indicates the theoretical moveout calculated by the best pair of splitting results of the Pms phase. **(D)** The green line indicates the theoretical moveout calculated after correcting the Pms arrivals with the upper crustal anisotropy results.

FIGURE 5
Crustal anisotropy results estimated in the study. The station numbers are shown near the stations. The orientation and length of the colorful bars denote φ and δt, respectively. The radiuses of the white circles are proportional to δt. The yellow bar denotes the measurement of the upper crust, and th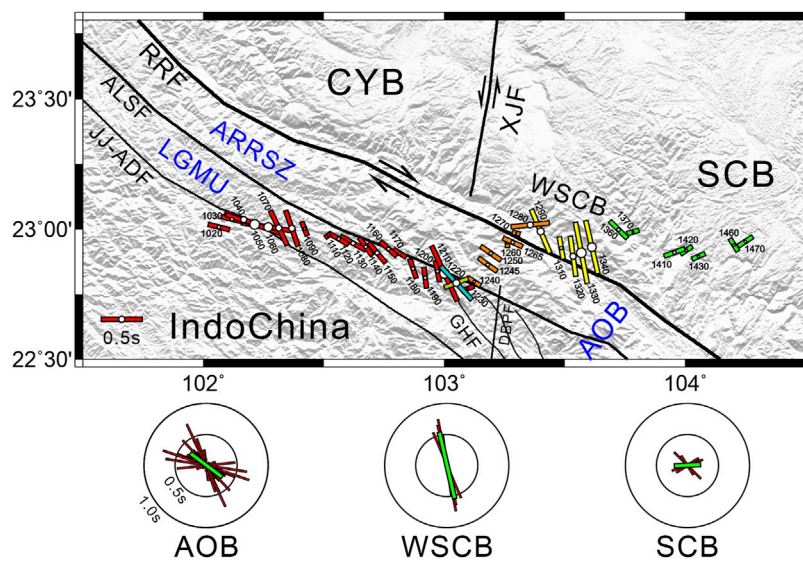e blue bar represents the anisotropy of the lower crust. The red, orange, light yellow, and green bars in the topographic map represent the measurements of LGMU, ARRSZ, WSCB, and SCB, respectively. The abbreviations for place names are referenced in the legend of Figure 1. The rose diagrams exhibit the distributions of fast directions in the AOB, WSCB, and SCB. The green bars represent the average anisotropy measurements in each region.

analysis, the layer stripping method is only employed at stations with well-covered Baz data, and clear Pis and Pms arrivals. Only the center station 1,220 meets the requirements. The measurements of the two-layered anisotropy is shown in Figure 4.

2.4 Quantification of the uncertainties of crustal anisotropy measurements

To quantify uncertainties, we employ the bootstrap approach to calculate the anisotropy results ten times randomly using 80% of the RFs, from which we derive σ_{φ} and $\sigma_{\delta t}$, representing the standard deviations of φ and δt, respectively. A combined standard deviation is obtained for each station according to the Eq. 2:

$$\sigma = \frac{\sigma_{\varphi}}{90.0} + \frac{\sigma_{\delta t}}{1.0} \qquad (2)$$

We exclude the stations having a σ greater than 0.4 (Kong et al., 2016). In addition, insufficient Baz coverage could introduce significant errors in the measurements. We retained only the stations with more than 6 out of 12 bands (each band covers a range of 30°), and required that the maximum Baz gap should be less than 180° (Zheng et al., 2018).

3 Results

After analyzing 49 center stations (referred to as "station" in the following text), we obtained reliable anisotropy parameters for a total of 40 stations including the station 1,220 with two layered anisotropy pattern (Figure 5; Table 1). Our results approximately agree with earlier findings nearby our stations (Sun et al., 2012; Chen et al., 2013;

Cai et al., 2016), but the study benefits from denser observations in the Ailaoshan Orogenic Belt, enabling a better investigation of the lateral variations in crustal deformation. The splitting parameters show obviously lateral variations. The fast directions have a clear correlation with the strikes of large-scale surface features with an arithmetic average of 125° ± 37°. The delay times vary from 0.07 to 0.75 s with a mean value of 0.33 ± 0.19 s. According to the major geological units, the study region is divided to 3 regions, the Ailaoshan Orogenic Belt, the western boundary of South China Block, and the South China Block. The regional averaged crustal anisotropy parameters are presented in Supplementary Table S1.

3.1 The Ailaoshan Orogenic Belt (AOB)

The AOB is located between the Yangtze-South China Block and Lanping-Simao Basin. The Jiujia-Anding Fault and the Red River Fault (RRF) respectively form its western and eastern boundaries. Based on the different deformation-metamorphism histories, the AOB can be featured by two separate tectonic units, the ARRSZ which is high-grade massif, and the low-grade metamorphic unit (LGMU) (Liu et al., 2015). The Ailaoshan Fault separates the two tectonic units. The fast directions in the AOB are primarily NW-SE, aligning with the strike of the major faults. The average value of delay times is 0.32 ± 0.18 s. The ARRSZ is sampled by stations 1,240 to 1,280 with a mean delay time of 0.24 ± 0.13 s. The LGMU has a larger averge delay time of 0.35 ± 0.19 s for stations 1,020 to 1,230. The station 1,220 is the only station along the profile that exhibits two layered crustal anisotropy. The upper crustal fast direction is oriented ENE-WSW which is oblique to the fault strike, while that for the lower crust roughly agrees with the Ailaoshan Fault strike. The delay time of the lower crust (0.55 s) is approximately twice that of the upper crust (0.31 s).

TABLE 1 Crustal anisotropy parameters.

Station	φ (°)	err$_φ$ (°)	δt (s)	err$_{δt}$ (s)	σ	Latitude (°)	Longitude (°)
1020	104	10	0.26	0.04	0.15	23.008	102.065
1030	104	6	0.26	0.06	0.13	23.038	102.119
1040	112	5	0.49	0.06	0.12	23.036	102.167
1050	109	2	0.73	0.03	0.05	23.018	102.213
1060	99	5	0.66	0.04	0.1	23.009	102.270
1070	154	3	0.47	0.07	0.1	23.005	102.312
1080	161	3	0.45	0.06	0.09	23.004	102.367
1090	158	6	0.18	0.05	0.12	23.001	102.421
1110	52	21	0.07	0.04	0.28	22.975	102.517
1120	120	8	0.28	0.07	0.16	22.962	102.561
1130	119	4	0.35	0.04	0.09	22.946	102.621
1140	144	7	0.26	0.06	0.14	22.932	102.673
1150	140	3	0.32	0.03	0.07	22.909	102.721
1160	132	6	0.26	0.04	0.11	22.924	102.769
1170	123	5	0.18	0.04	0.09	22.908	102.816
1180	161	6	0.24	0.04	0.11	22.849	102.870
1190	173	6	0.25	0.11	0.18	22.813	102.921
1200	169	13	0.25	0.2	0.35	22.838	102.971
1210	155	3	0.73	0.01	0.04	22.830	103.001
1220 upper	69	4	0.31	0.04	0.09	22.793	103.049
1220 lower	137	4	0.55	0.07	0.12	22.793	103.049
1230	69	26	0.16	0.06	0.35	22.771	103.097
1240	123	5	0.18	0.06	0.11	22.798	103.124
1245	126	3	0.28	0.03	0.06	22.864	103.180
1250	125	6	0.3	0.02	0.09	22.907	103.193
1260	180	19	0.1	0.08	0.29	22.945	103.261
1265	114	20	0.25	0.13	0.36	22.950	103.284
1270	105	19	0.1	0.08	0.29	22.984	103.298
1280	84	23	0.47	0.07	0.33	23.017	103.355
1290	157	3	0.57	0.09	0.12	22.992	103.399
1310	170	21	0.28	0.1	0.34	22.927	103.485
1320	172	4	0.49	0.06	0.1	22.896	103.534
1330	169	10	0.75	0.12	0.23	22.909	103.568
1340	167	20	0.66	0.09	0.31	22.931	103.613
1360	135	9	0.3	0.06	0.16	22.998	103.722
1370	75	21	0.15	0.09	0.32	22.990	103.782
1410	70	10	0.26	0.08	0.18	22.910	103.955
1420	56	7	0.17	0.08	0.16	22.919	104.003

(Continued on following page)

TABLE 1 (*Continued*) Crustal anisotropy parameters.

Station	φ (°)	err$_φ$ (°)	δt (s)	err$_{δt}$ (s)	σ	Latitude (°)	Longitude (°)
1430	66	13	0.17	0.14	0.28	22.896	104.055
1460	148	27	0.18	0.04	0.35	22.939	104.202
1470	57	15	0.21	0.03	0.2	22.953	104.249

err$_φ$ and err$_{δt}$ represent standard deviations of φ and δt, respectively. Lat and Lon represent the latitude and longitude of the station, respectively.

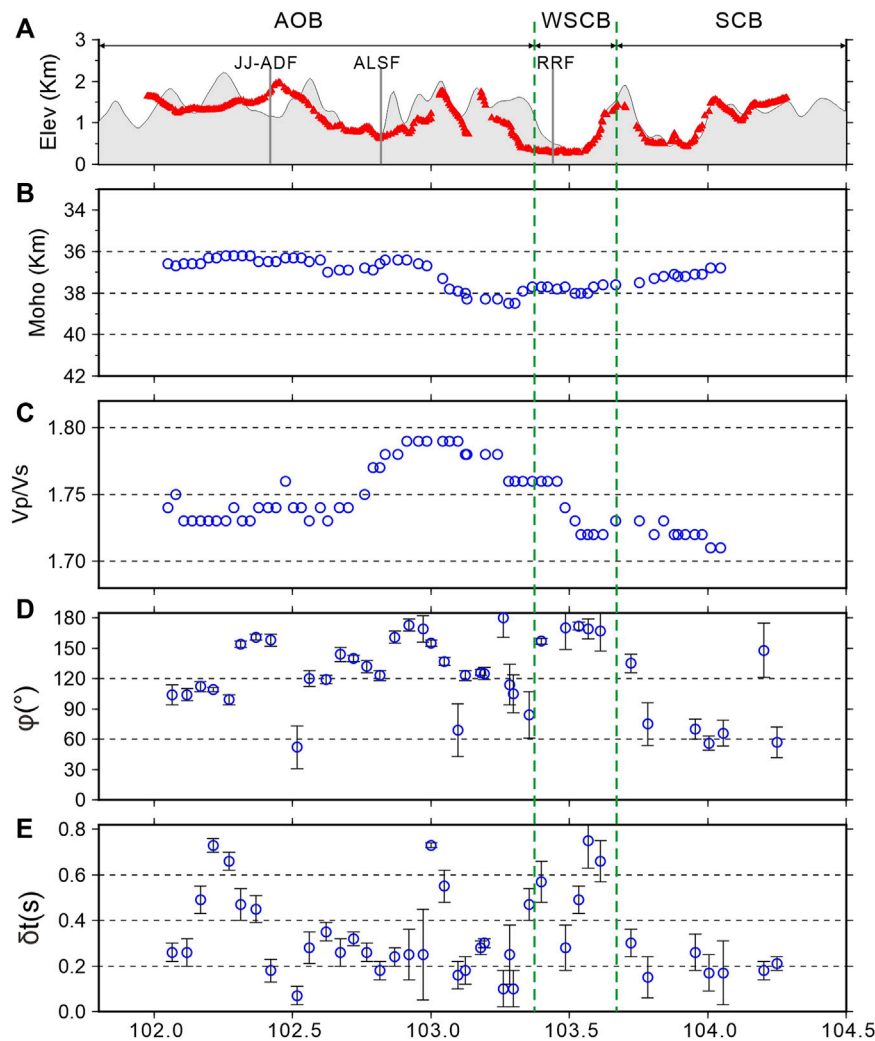FIGURE 6
Two-dimensional section of topography **(A)**, Moho depth **(B)**, Vp/Vs ratios **(C)**, fast directions **(D)** and delay times **(E)**. The data in **(B,C)** are the H-κ stacking results (Zhang et al., 2020). The results in **(D,E)** are crustal anisotropy measurements in this study. The region is divided into the AOB, WSCB, and SCB by the two green dashed lines. The abbreviations for place names are referenced in the legend of Figure 1.

3.2 The west boundary of South China Block (WSCB)

The WSCB region is sampled by the stations 1,290 to 1,340. The fast directions are dominantly N-S, which do not agree with the strike of the RRF. This region has the largest mean delay time of 0.55 ± 0.18 s.

3.3 The South China block (SCB)

The tectonically stable SCB is characterized by the smallest average delay time of 0.21 ± 0.06 s, sampled by the stations 1,360 to 1,470. The fast directions are primarily oriented ENE-WSW, with some also oriented NW-SE.
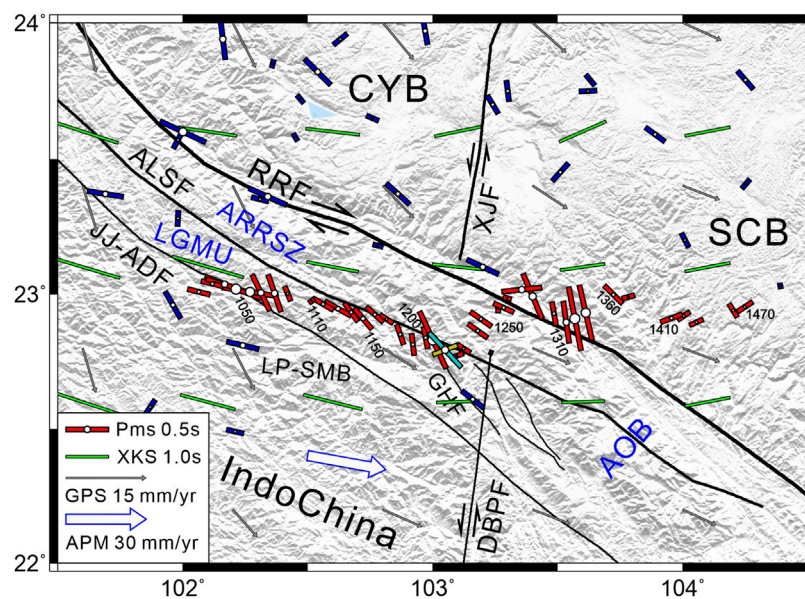
FIGURE 7
Comparison of the crustal anisotropy results in the study with other measurements. The orientation and length of the red bars denote φ and δt, respectively. The yellow bar denotes the upper crustal anisotropy, and the blue bar represents the lower crustal anisotropy. The deep blue bars represent the crustal anisotropy measurements of previous studies (Sun et al., 2012; Chen et al., 2013; Cai et al., 2016). The green bars represent area-averaged XKS splitting parameters (Shi et al., 2012; Wang et al., 2013; Huang et al., 2015). The gray arrows denote the area-averaged GPS results (Gan et al., 2007). The white arrow shows the Absolute Plate Motion (APM) (Kreemer et al., 2014).

4 Discussion

4.1 Major source to the crustal anisotropy

Given that the Pms phase originates at the Moho and follows raypaths limited to the crust, the splitting parameters of Pms offer direct insights into the anisotropy and deformation occurring throughout the entire crust. Except for the station 1,220 which has two layered anisotropy, the results of other stations reflect the whole crustal anisotropy, making it challenging to determine the primary source of anisotropy. Luckily, Shi et al. (2012) analyzed the local S splitting based on the seismograms from the Yunnan seismograph network. They revealed that the delay time is 1.65 ms/km in the SCB near our seismic profile. Using the data from the stations of ChinArray, Tai et al. (2015) obtained a larger delay time of 4.22 ms/km for the ARRSZ. Because the earthquake depth in this region is usually less than 10–15 km, located in the upper crust, we can conclude that the delay time of the upper crust is 0.02 s and 0.06 s in SCB and ARRSZ, respectively. In contrast, we observed a delay time of 0.21 s in the SCB and of 0.32 s in ARRSZ, and we can deduce that the contribution of the upper crust to the delay time is less than 1/5 of the entire crust. Hence, we suggest that the anisotropy beneath the study area primarily comes from the middle-lower crust, making it a specific indicator of deformation occurring within the middle-lower crust.

4.2 Formation mechanisms for the detected crustal anisotropy

The dense array with intervals of 5 km for center stations offers an excellent opportunity for investigating the crustal anisotropy

and deformation pattern of AOB. The crustal anisotropy of AOB is significantly influenced by the ARRSZ. The large-scale left-lateral shear occurred along the ARRSZ between the Oligocene and Early Miocene, later succeeded by a shift to right-lateral in the Late Miocene (Shi et al., 2018). The strong shear induced the anisotropic minerals' LPO in the mid-lower crust, inducing the strike-parallel anisotropy. Regarding the potential expansion of shear zones at deeper levels, the regional presence of aligned minerals may extend to widths of several tens of kilometers perpendicular to the fault (Lockett and Kusznir, 1982). The intracrustal discontinuities dipping westward beneath the ARRSZ suggest the westward extension of the shear zone at depth, resulting in the crustal anisotropy under the LGMU. The shear heating resulting from the relative motion along strike-slip faults and mantle upwelling caused by lithospheric delamination since ~35 Ma may both play a role in reducing the velocity and producing partial melting of the middle-lower crust as well as the increased Vp/Vs ratio of the AOB (Figure 6) (Xu et al., 2022; Xu et al., 2023). The delay times span from 0.07 s to 0.73 s, indicating that the shear strength is variable. The crustal anisotropy near the Ganhe Fault is influenced by the fault, changing from NW-SE to NNW-SSE. For the station 1,220, the ENE-WSW oriented fast direction is consistent with the upper crustal anisotropy by Han et al. (2020) who applied the harmonic decomposition approach. The measurement appears to have no significant correlation with the fault strike or the near N-S maximum horizontal compression. Intense shear strains are concentrated in the intersection area of several faults, where varying pore pressures could lead to alterations in the crack orientations because of the closure of fluid-saturated micro-cracks (Crampin and Peacock, 2008).

The strongest crustal anisotropy is observed in the western margin of the SCB. The fast directions align with the maximum horizontal compression, indicating that the observed anisotropy is attributed to the extensional fluid-saturated micro-cracks. However, it is difficult for the stress-induced anisotropy to generate such a large delay time of 0.55 s. The N-S oriented Xiaojiang Fault is the boundary fault between the Central Yunnan Block and the SCB. The GPS observations show that the left-lateral motion is ~10 mm/yr (Gan et al., 2007). In addition, the stations located near the fault exhibit strike-parallel crustal anisotropy, indicating that the strike-slip motion could influence the entire crust (Cai et al., 2016). The fast strike-slip motion may cause the alignment of the minerals of the middle-lower crust beneath the WSCB, causing the N-S oriented fast direction. Moreover, the NNE-trending Dien Bien Phu Fault (DBPF) south of the RRF, is suggested as a reactivated fault that accommodated the tectonic shear transferred from the XJF across the RRF since the Pliocene (Lai et al., 2012). The left lateral motion of the DBPF may also contribute to the crustal anisotropy of WSCB. Accordingly, the strong crustal anisotropy of WSCB is a result of the combined influence of crustal stress and tectonics. The westward inclination of the intracrustal interfaces and the low-velocity zones may indicate the westward extension of the shear zone, and there are no distinct fault features beneath the RRF (Zhang et al., 2020; Xu et al., 2022). Thus it suggests that the RRF may not have a significant impact on the crustal anisotropy in this region.

The relatively smaller delay times in the SCB indicate that the crustal anisotropy is quite weak. The shear wave velocity models from ambient noise studies show that the high-velocity anomaly exists in the middle-lower crust beneath the SCB (Bao et al., 2015; Qiao et al., 2018), suggesting the rigidness of the SCB. Thus it may be difficult to produce intense deformation as well as associated crustal anisotropy, which is also supported by the flatter intracrustal discontinuities from the CCP image of this profile and weaker seismicity than adjacent areas (Zhang et al., 2020).

4.3 Implication for the crustal flow model

Based on the absence of surface shortening in the southeastern Tibetan Plateau, Royden et al. (1997) introduced the lower crustal flow concept. The mechanical weakness of the middle-lower crust has also been corroborated by some geophysical studies, including low-velocity zones (LVZs) within the crust (Yao et al., 2008), strong attenuation (Zhao et al., 2013), near N-S crustal azimuthal anisotropy (Sun et al., 2012; Chen et al., 2013), and elevated electrical conductivity (Bai et al., 2010). Some studies indicate the possible presence of two channels for crustal flow in southeastern Tibet (Bai et al., 2010; Sun et al., 2012; Zhao et al., 2013). Applying joint inversion of seismic data using ChinArray data, Bao et al. (2015) revealed a high-resolution distribution of LVZs and suggested there exist two channels of ductile flow. The one in the eastern channel flows southward and passes the AOB in the study region. The ambient noise tomography also observed the LVZs which represent crustal flow cross the RRF and extend to the south (Qiao et al., 2018). However, the eastern channel of the crustal flow inferred from low-Q_{Lg} belt terminates north of the RRF (Zhao et al., 2013). The crustal flow could result in the LPO of anisotropic minerals, generating significant anisotropy. Thus, the analysis of crustal anisotropy provides a valuable tool to assess the presence of crustal flow beneath this study area.

Some geophysical observations from our profile serve as evidence to exclude the presence of the crustal flow beneath the study area. At first, if the crustal flow exists, the fast direction would be oriented N-S or NNE-SSW as predicted by the clockwise rotation of material around the eastern Himalaya syntaxis. However beneath the AOB, the NW-SE oriented fast directions generally align with the strike of nearby faults. Then, the significant lateral variation in the splitting parameters, including delay times ranging from 0.07 s to 0.75 s, and the fast directions changing by over 70° near the RRF, contradict the presence of large-scale crustal flow. In addition, a Vp/Vs ratio of 2.0 is regarded as the minimum threshold for crustal flow (Jamieson et al., 2011), while the remainder of the crust maintains a ratio of 1.77 (Christensen, 1996). The estimates show that a crustal flow layer of 10–20 km would elevate the average Vp/Vs to 1.83 to 1.89, significantly higher than the average ratio of 1.75 in the AOB (Figure 6), which does not support the crustal flow model.

4.4 Implication for the deformation pattern

Previous studies compared observations from multidisciplinary studies to analyze the deformation pattern of crust and mantle, including surface geological features, GPS velocities, Pms sinusoidal moveout, XKS splitting analysis, and absolute plate motion (APM). For the area south of 26° N, XKS fast directions change to generally E-W orientation (Huang et al., 2015). Based on the XKS fast directions parallel to the maximum extension in the crust inferred from GPS and geological data inversion, Wang et al. (2008) argued the coupling between the crust and mantle, which is supported by Huang et al. (2015) using XKS splitting analysis to the ChinArray. However, the information from GPS only represents the deformation in shallow crust. Comparing Pms and XKS anisotropy parameters should be a better choice because they indicate the anisotropy and related deformation for crust and mantle, respectively. According to the Pms as well as XKS splitting parameters for several permanent stations, Sun et al. (2012) argued that there exists lower crustal flow which mechanically decouples the mantle lithosphere from the upper crust. Cai et al. (2016) also supported the decoupling model, however, they attributed the anisotropy to the strike-slip motion near the primary faults rather than the ductile flow.

The average Pms fast directions in the AOB and WSCB are oriented NW-SE and NNW-SSE, respectively, primarily caused by the shear effect of the strike-slip faults. The nearly E-W oriented upper mantle anisotropy from XKS splitting may be caused by the lithospheric deformation when the collapsing lithosphere encounters resistance from the surrounding medium (Wang et al., 2008) or asthenospheric flow inferred from APM (Figure 7) (Huang et al., 2015). The difference between the Pms and XKS splitting parameters indicates a decoupling deformation between the crust and mantle. For the SCB, the consistency between the two fast directions probably suggests crust-mantle coupling, but further data in the future would be necessary to confirm this. Thus, in the study region, we favor that the block extrusion pattern controlled by active boundary faults is the dominant mode of

deformation in the region, but it occurs only at the crustal scale, supported by the relatively flat Moho (Figure 5).

5 Conclusion

To better understand the lateral growth of the Tibetan Plateau, we measure the detailed crustal anisotropy from Pms phase of the receiver functions utilizing seismic data from a short-period dense array across the Ailaoshan Orogenic Belt in southeastern Tibet. Our findings reveal the significant crustal anisotropy across the entire study area, characterized by a mean delay time of 0.33 ± 0.19 s, indicating that the crustal anisotropy primarily lies within the middle-lower crust. The generally NW-SE oriented fast directions beneath the ARRSZ and its western low-grade metamorphic unit align with the strike of ARRSZ, suggesting the anisotropy is predominantly a result of the strike-slip motion along the shear zone. In contrast, we find that the South China Block exhibits weak crustal anisotropy implying limited internal deformation. The N-S oriented anisotropy beneath the western boundary of SCB is likely affected by both crustal stress and the Xiaojiang Fault. Based on the high Vp/Vs ratios and obvious lateral variations in crustal anisotropy, we propose that the strike-slip motion along the ARRSZ leads to partial melting and notable crustal anisotropy in the middle-lower crust beneath the AOB, without the presence of crustal flow. The differences between crustal and mantle anisotropy suggest that the crustal deformation is decoupled from the upper mantle under the AOB, which supports the block extrusion model limited to the crustal scale as the primary deformation pattern.

Data availability statement

The original contributions presented in the study are included in the Supplementary Material, further inquiries can be directed to the corresponding author.

Author contributions

CW: Conceptualization, Formal Analysis, Investigation, Methodology, Writing–original draft, Writing–review and editing.

TX: Writing–review and editing, Funding acquisition, Supervision. ZB: Supervision, Writing–review and editing, Data curation.

Conflict of interest

The authors declare that the research was conducted in the absence of any commercial or financial relationships that could be construed as a potential conflict of interest.

Publisher's note

All claims expressed in this article are solely those of the authors and do not necessarily represent those of their affiliated organizations, or those of the publisher, the editors and the reviewers. Any product that may be evaluated in this article, or claim that may be made by its manufacturer, is not guaranteed or endorsed by the publisher.

Supplementary material

The Supplementary Material for this article can be found online at: https://www.frontiersin.org/articles/10.3389/feart.2023.1343474/full#supplementary-material

References

Bai, D., Unsworth, M. J., Meju, M. A., Ma, X., Teng, J., Kong, X., et al. (2010). Crustal deformation of the eastern Tibetan plateau revealed by magnetotelluric imaging. *Nat. Geosci.* 3 (5), 358–362. doi:10.1038/ngeo830

Bao, X., Sun, X., Xu, M., Eaton, D. W., Song, X., Wang, L., et al. (2015). Two crustal low-velocity channels beneath SE Tibet revealed by joint inversion of Rayleigh wave dispersion and receiver functions. *Earth Planet. Sci. Lett.* 415, 16–24. doi:10.1016/j.epsl.2015.01.020

Boness, N. L., and Zoback, M. D. (2006). Mapping stress and structurally controlled crustal shear velocity anisotropy in California. *Geology* 34 (10), 825–828. doi:10.1130/g22309.1

Cai, Y., Wu, J., Fang, L., Wang, W., and Yi, S. (2016). Crustal anisotropy and deformation of the southeastern margin of the Tibetan Plateau revealed by Pms splitting. *J. Asian Earth Sci.* 121, 120–126. doi:10.1016/j.jseaes.2016.02.005

Chen, Y., Zhang, Z., Sun, C., and Badal, J. (2013). Crustal anisotropy from Moho converted Ps wave splitting analysis and geodynamic implications beneath the eastern

margin of Tibet and surrounding regions. *Gondwana Res.* 24 (3-4), 946–957. doi:10.1016/j.gr.2012.04.003

Christensen, N. I. (1996). Poisson's ratio and crustal seismology. *J. Geophys. Res. Solid Earth* 101 (B2), 3139–3156. doi:10.1029/95jb03446

Clark, M. K., and Royden, L. H. (2000). Topographic ooze: building the eastern margin of Tibet by lower crustal flow. *Geology* 28 (8), 703–706. doi:10.1130/0091-7613(2000)28<703:tobtem>2.0.co;2

Crampin, S. (1991). Wave propagation through fluid-filled inclusions of various shapes: interpretation of extensive-dilatancy anisotropy. *Geophys. J. Int.* 104 (3), 611–623. doi:10.1111/j.1365-246x.1991.tb05705.x

Crampin, S., and Peacock, S. (2008). A review of the current understanding of seismic shear-wave splitting in the Earth's crust and common fallacies in interpretation. *Wave Motion* 45 (6), 675–722. doi:10.1016/j.wavemoti.2008.01.003

England, P., and McKenzie, D. (1982). A thin viscous sheet model for continental deformation. *Geophys. J. Int.* 70 (2), 295–321. doi:10.1111/j.1365-246x.1982.tb04969.x

Gan, W., Zhang, P., Shen, Z. K., Niu, Z., Wang, M., Wan, Y., et al. (2007). Present-day crustal motion within the Tibetan Plateau inferred from GPS measurements. *J. Geophys. Res. Solid Earth* 112 (B8). doi:10.1029/2005jb004120

Gao, Y., Wu, J., Fukao, Y., Shi, Y., and Zhu, A. (2011). Shear wave splitting in the crust in North China: stress, faults and tectonic implications. *Geophys. J. Int.* 187 (2), 642–654. doi:10.1111/j.1365-246x.2011.05200.x

Han, C., Xu, M., Huang, Z., Wang, L., Xu, M., Mi, N., et al. (2020). Layered crustal anisotropy and deformation in the SE Tibetan plateau revealed by Markov-Chain-Monte-Carlo inversion of receiver functions. *Phys. Earth Planet. Inter.* 306, 106522. doi:10.1016/j.pepi.2020.106522

Huang, Z., Wang, L., Xu, M., Ding, Z., Wu, Y., Wang, P., et al. (2015). Teleseismic shear-wave splitting in SE Tibet: insight into complex crust and upper-mantle deformation. *Earth Planet. Sci. Lett.* 432, 354–362. doi:10.1016/j.epsl.2015.10.027

Jamieson, R. A., Unsworth, M. J., Harris, N. B., Rosenberg, C. L., and Schulmann, K. (2011). Crustal melting and the flow of mountains. *Elements* 7 (4), 253–260. doi:10.2113/gselements.7.4.253

Kennett, B., and Engdahl, E. (1991). Traveltimes for global earthquake location and phase identification. *Geophys. J. Int.* 105 (2), 429–465. doi:10.1111/j.1365-246x.1991.tb06724.x

Kong, F., Wu, J., Liu, K. H., and Gao, S. S. (2016). Crustal anisotropy and ductile flow beneath the eastern Tibetan Plateau and adjacent areas. *Earth Planet. Sci. Lett.* 442, 72–79. doi:10.1016/j.epsl.2016.03.003

Kreemer, C., Blewitt, G., and Klein, E. C. (2014). A geodetic plate motion and global strain rate model. *Geochem. Geophys., Geosystems* 15 (10), 3849–3889. doi:10.1002/2014gc005407

Lai, K.-Y., Chen, Y.-G., and Lâm, D. Đ. (2012). Pliocene-to-present morphotectonics of the dien bien Phu Fault in northwest vietnam. *Geomorphology* 173, 52–68. doi:10.1016/j.geomorph.2012.05.026

Li, J., Song, X., Wang, P., and Zhu, L. (2019). A generalized H-κ method with harmonic corrections on Ps and its crustal multiples in receiver functions. *J. Geophys. Res. Solid Earth* 124 (4), 3782–3801. doi:10.1029/2018jb016356

Liu, H., and Niu, F. (2012). Estimating crustal seismic anisotropy with a joint analysis of radial and transverse receiver function data. *Geophys. J. Int.* 188 (1), 144–164. doi:10.1111/j.1365-246x.2011.05249.x

Liu, J., Chen, X., Wu, W., Tang, Y., Tran, M.-D., Nguyen, Q.-L., et al. (2015). New tectono-geochronological constraints on timing of shearing along the Ailao Shan-Red River shear zone: implications for genesis of Ailao Shan gold mineralization. *J. Asian Earth Sci.* 103, 70–86. doi:10.1016/j.jseaes.2014.11.006

Lockett, J., and Kusznir, N. (1982). Ductile shear zones: some aspects of constant slip velocity and constant shear stress models. *Geophys. J. Int.* 69 (2), 477–494. doi:10.1111/j.1365-246x.1982.tb04961.x

Qiao, L., Yao, H., Lai, Y. C., Huang, B. S., and Zhang, P. (2018). Crustal structure of Southwest China and northern Vietnam from ambient noise tomography: implication for the large-scale material transport model in SE Tibet. *Tectonics* 37 (5), 1492–1506. doi:10.1029/2018tc004957

Royden, L. H., Burchfiel, B. C., King, R. W., Wang, E., Chen, Z., Shen, F., et al. (1997). Surface deformation and lower crustal flow in eastern Tibet. *Science* 276 (5313), 788–790. doi:10.1126/science.276.5313.788

Rümpker, G., Kaviani, A., and Latifi, K. (2014). Ps-splitting analysis for multilayered anisotropic media by azimuthal stacking and layer stripping. *Geophys. J. Int.* 199 (1), 146–163. doi:10.1093/gji/ggu154

Shi, X., Sieh, K., Weldon, R., Zhu, C., Han, Y., Yang, J., et al. (2018). Slip rate and rare large prehistoric earthquakes of the Red River fault, southwestern China. *Geochem. Geophys., Geosystems* 19 (7), 2014–2031. doi:10.1029/2017gc007420

Shi, Y., Gao, Y., Su, Y., and Wang, Q. (2012). Shear-wave splitting beneath yunnan area of southwest China. *Earthq. Sci.* 25, 25–34. doi:10.1007/s11589-012-0828-4

Shi, Y., Gao, Y., Zhang, H., Zhang, Z., and Li, G. (2023). Crustal azimuthal anisotropy in the lateral collision zone of the SE margin of the Tibetan Plateau and its tectonic implications. *Geophys. J. Int.* 234 (1), 1–11. doi:10.1093/gji/ggad059

Sun, Y., Niu, F., Liu, H., Chen, Y., and Liu, J. (2012). Crustal structure and deformation of the SE Tibetan plateau revealed by receiver function data. *Earth Planet. Sci. Lett.* 349, 186–197. doi:10.1016/j.epsl.2012.07.007

Tai, L.-X., Gao, Y., Liu, G., and Xiao, Z. (2015). Crustal seismic anisotropy in the southeastern margin of Tibetan Plateau by ChinArray data: shear-wave splitting from temporary observations of the first phase. *Chin. J. Geophys.* 58 (11), 4079–4091. doi:10.6038/cjg20151116

Tan, P., and Nie, S. (2021). Crustal deformation in eastern margin of Tibetan Plateau from a dense linear seismic array. *Phys. Earth Planet. Inter.* 321, 106801. doi:10.1016/j.pepi.2021.106801

Tapponnier, P., Xu, Z., Roger, F., Meyer, B., Arnaud, N., Wittlinger, G., et al. (2001). Oblique stepwise rise and growth of the Tibet Plateau. *Science* 294 (5547), 1671–1677. doi:10.1126/science.105978

Wang, C. Y., Flesch, L. M., Chang, L., and Zheng, T. (2013). Evidence of active mantle flow beneath South China. *Geophys. Res. Lett.* 40 (19), 5137–5141. doi:10.1002/grl.50987

Wang, C.-Y., Flesch, L. M., Silver, P. G., Chang, L.-J., and Chan, W. W. (2008). Evidence for mechanically coupled lithosphere in central Asia and resulting implications. *Geology* 36 (5), 363–366. doi:10.1130/g24450a.1

Wu, C., Tian, X., Xu, T., Liang, X., Chen, Y., Zhu, G., et al. (2019). Upper-crustal anisotropy of the conjugate strike-slip fault zone in central Tibet analyzed using local earthquakes and shear-wave splitting. *B. Seismol. Soc. Am.* 109 (5), 1968–1984. doi:10.1785/0120180333

Wu, C., Xu, T., Ai, Y., Dong, W., Li, L., and Hou, J. (2021). Crustal azimuthal anisotropy in the jiaodong peninsula: evidence for the suture between the north China craton and south China block. *Phys. Earth Planet. Inter.* 314, 106705. doi:10.1016/j.pepi.2021.106705

Xu, M., Wang, K., Chen, J., Yu, D., and Tong, P. (2023). Receiver function adjoint tomography for three-dimensional high-resolution seismic array imaging: methodology and applications in southeastern Tibet. *Geophys. Res. Lett.* 50 (19), e2023GL104077. doi:10.1029/2023gl104077

Xu, M., Yu, D., Huang, Z., Tong, P., Hao, S., Ruan, Y., et al. (2022). Crustal and uppermost mantle heterogeneities across the Ailaoshan Red River shear zone, SE Tibet: implications for Cenozoic magmatic activity. *J. Geophys. Res. Solid Earth* 127 (6), e2021JB023656. doi:10.1029/2021jb023656

Yang, Y., Zhang, X., Dong, Y., Sun, S., Hua, Q., and Liang, C. (2022). Crustal deformation patterns in the Tibetan plateau and its adjacent regions as revealed by receiver functions. *B. Seismo. Soc. Am.* 112 (3), 1297–1314. doi:10.1785/0120210228

Yao, H., Beghein, C., and Van Der Hilst, R. D. (2008). Surface wave array tomography in SE Tibet from ambient seismic noise and two-station analysis-II. Crustal and upper-mantle structure. *Geophys. J. Int.* 173 (1), 205–219. doi:10.1111/j.1365-246x.2007.03696.x

Yin, A., and Harrison, T. M. (2000). Geologic evolution of the Himalayan-Tibetan orogen. *Annu. Rev. earth Pl. sc.* 28 (1), 211–280. doi:10.1146/annurev.earth.28.1.211

Zhang, L., Bai, Z., Xu, T., Wu, Z., Huang, M., Yu, G., et al. (2020). Cenozoic magmatic activity and oblique uplifting of the Ailao Mountain: evidence from a short-period dense seismic array. *Sci. China Earth Sci.* 63, 1294–1308. doi:10.1007/s11430-019-9616-y

Zhao, L.-F., Xie, X.-B., He, J.-K., Tian, X., and Yao, Z.-X. (2013). Crustal flow pattern beneath the Tibetan Plateau constrained by regional Lg-wave Q tomography. *Earth Planet. Sci. Lett.* 383, 113–122. doi:10.1016/j.epsl.2013.09.038

Zheng, M., Bai, Z., Xu, T., and Badal, J. (2021). Upper crustal velocity structure of the Ailaoshan-Red River shear zone and its implication for Cenozoic tectonic-magmatic activity: evidence from ambient noise tomography using short-period dense seismic array. *Phys. Earth Planet. Inter.* 311, 106643. doi:10.1016/j.pepi.2021.106643

Zheng, T., Ding, Z., Ning, J., Chang, L., Wang, X., Kong, F., et al. (2018). Crustal azimuthal anisotropy beneath the southeastern Tibetan Plateau and its geodynamic implications. *J. Geophys. Res. Solid Earth* 123 (11), 9733–9749. doi:10.1029/2018jb015995